Valence band position and photocatalytic properties based on different morphologies of Bi_2WO_6

Hao Zhou[a], Fengjun Zhang[a], Jibo Han[a], Xinjing Peng[a,c,*], Shuang Zhong[a,b,d,*]

[a]*Key Laboratory of Groundwater Resources and Environment, Ministry of Education, Jilin University, Changchun 130021, China, Tel. +86 17743013233; email: pengxinjing1985@163.com (X. Peng), zhongshuang13@hotmail.com (S. Zhong), 954452688@qq.com (H. Zhou), zhangfengjun@jlu.edu.cn (F. Zhang), 1045273883@qq.com (J. Han)*
[b]*Key Laboratory of Songliao Aquatic Environment, Ministry of Education, Jilin University, Changchun 130018, China*
[c]*College of Environment and Safety Engineering, Shenyang University of Chemical Technology, Shenyang 110142, China*
[d]*Institute of Water Resources and Environment, Jilin University, Changchun 130021, China*

ABSTRACT

Different morphological forms of bismuth tungstate (Bi_2WO_6) catalysts, termed P-Bi_2WO_6, R-Bi_2WO_6, Q-Bi_2WO_6, and W-Bi_2WO_6 were prepared by a variety of methods. Photocatalyst samples were characterized by scanning electron microscopy as well as energy-dispersive, X-ray photoelectron, ultraviolet/visible spectroscopies, photoluminescence spectra, and the Brunauer–Emmett–Teller method. The photocatalytic activities of the Bi_2WO_6 catalysts were determined by photocatalytic degradation of rhodamine B in aqueous solution under visible light irradiation. Photocatalytic degradation experiments showed that P-Bi_2WO_6 had the best photocatalytic effects among these catalysts, with a degradation rate of 94.82% within 150 min of irradiation. Based on comprehensive analyses of the characterization and photocatalytic experiments, the results showed that P-Bi_2WO_6 had the highest valence band (2.71 eV) and lowest forbidden bandwidth (2.45 eV), such that its visible light response was stronger than the other forms. After four cycles, the degradation efficiency decreased by only 2.24%, which revealed the relatively high photostability of P-Bi_2WO_6. These results indicated that the higher the Bi_2WO_6 valence band position was, the better the oxidation activity. This study provided a theoretical basis for future research into Bi_2WO_6 photocatalysis.

Keywords: Visible light response; Photocatalyst; Bismuth tungstate; Morphology valence band

1. Introduction

In recent years, the discharge of printing and dyeing wastewater has been increasing [1], and traditional wastewater treatment methods cannot meet the requirements of diversified wastewater treatment and, thus, treatment technology needs to be continuously improved [2]. The latest research shows that the degradation of organic dyes and antibiotics in polluted water through semiconductor photocatalysts has become the focus of current treatment techniques for printing and dyeing wastewater [3]. Photocatalytic technology can effectively utilize solar energy, being relatively cheap and environmentally friendly and with a high response to visible light [4,5].

The valence band position of a photocatalyst material is closely related to its oxidation activity. Li's group has recently found that an appropriate rGO ratio in nanocomposites leads to a noticeable positively-shifted valence band edge potential and significantly adjusts nanocomposite band structure, meaning increased oxidation power [6]. Zhang and co-workers have used *n*-type inorganic and organic semiconductor materials to form *n-n* heterojunctions and then

explained the mechanism for enhanced photocatalytic degradation. The position of the valence and conduction bands (VB and CB, respectively) between Bi_2WO_6 and PDI are conducive to heterojunction formation, thereby promoting the separation of photogenerated electrons and holes to improve catalytic performance [7]. Liu's group has reported the synthesis of bismuth titanate nanorods, with a cubic $Bi_2Ti_2O_7$ phase, by a facile hydrothermal process without any additives. The VB (2.60 eV) of the product was higher than that of alpha-Bi_2O_3 (2.83 eV) and the degradation activity toward methyl orange under illumination was much better than that of alpha-Bi_2O_3 and with better stability. The reason for this result was that the valence band of $Bi_{20}TiO_{32}$ was mainly composed of Bi-6s and O-2p orbitals and the valence band more dispersed. This facilitated the movement of photogenic carriers, hindered their recombination, and was beneficial to the improvement of photocatalytic and oxidation activities [8].

Therefore, combined with the study of band theory, it was speculated here that materials with a more dispersed and higher valence band were more favorable for photogenic hole migration and thus would have high catalytic performance and oxidation activity [9]. However, there have been few studies regarding the relationship between the Bi_2WO_6 valence band location and oxidation activity. Bi_2WO_6, one of the simplest members of the Aurivillius oxide family, is composed of a perovskite $[WO_4]^{2-}$ layer sandwiched between bismuth oxide $[Bi_2O_2]^{2+}$ layers, which is conducive to the effective separation of photogenerated electron-hole pairs and the enhancement of photocatalytic activity due to the formation of an internal electric field between the plates [3,10,11], making Bi_2WO_6 exhibit good photocatalytic performance under visible-light irradiation [12]. The band gap energy of Bi_2WO_6 is 2.38 eV and the valence band at 2.60 eV [13–15]. Density functional theory calculations have shown that the valence band (VB) is mainly formed by hybridization of O-2p with Bi-6s orbitals [16], which not only makes the VB largely dispersed, but also favors the mobility of photo-induced holes for specific oxidation reaction. The hybridization phenomenon of VB makes the Bi_2WO_6 valence band dispersed, potential increased [14], band gap narrowed, and photogenic holes in the VB faster-moving, thus strengthening the photocatalytic activity of Bi_2WO_6 [17–19].

In this study, based on previous studies, four different morphological forms of Bi_2WO_6 were prepared by a variety of methods, including block, flower ball, nest-like, and hexahedral Bi_2WO_6. Using optical and electrochemical techniques, the four different materials were examined in detail regarding their conduction and VB location in Bi_2WO_6. Combined with experiments regarding the photocatalytic degradation of rhodamine B (RhB), the different morphologies of photocatalytic materials based on VB position and the relationship with oxidation catalytic ability were comprehensively analyzed and verified.

2. Materials and methods

2.1. Materials

All materials used in this study were of analytical grade and used without further purification. $Bi(NO_3)_3 \cdot 5H_2O$, $Na_2WO_4 \cdot 2H_2O$, ethylene glycol (EG), sodium dodecylbenzene sulfonate (SDBS), Na_2SO_4, and H_2SO_4 were provided by the Sinopharm Chemical Reagent Co. Ltd., (Shanghai, China). NaOH was obtained from Tianjin Guangfu Technology Development Co., (Tianjin, China). Distilled water was used in all experiments.

2.2. Synthesis of different Bi_2WO_6 catalysts

2.2.1. Synthesis of P-Bi_2WO_6 nanostructures

The P-Bi_2WO_6 catalyst was obtained by a reported method [20]. Typically, 1.00 wt.% SDBS was dissolved in 40.00 mL of EG and stirred until fully dissolved. Then, 4.0 mmol of $Bi(NO_3)_3 \cdot 5H_2O$ was added and stirred until fully dissolved to obtain solution A. Meanwhile, 2.0 mmol (0.6596 g) of $Na_2WO_4 \cdot 2H_2O$ was dissolved into 30.00 mL EG to obtain solution B. Then, solution B was slowly injected into solution A and stirring for 1 h. The resulting mixture was transferred to a 100 mL Teflon-lined autoclave, which was then sealed and heated to 180°C for 16 h. The product was naturally cooled to room temperature and the solid precipitate filtered, washed with ethyl alcohol and distilled water 3–5 times, and dried at 60°C for 6 h.

2.2.2. Synthesis of R-Bi_2WO_6

The R-Bi_2WO_6 catalyst was obtained using a reported method [21]. Here, 0.5 mmol of $Na_2WO_4 \cdot 2H_2O$ was dissolved in 60 mL of deionized water and stirred for 20 min to form solution A. Next, 1 mmol of $Bi(NO_3)_3$ was dissolved in 5 mL of glacial acetic acid with magnetic stirring at room temperature until complete dissolution, to form solution B. Then, solution B was poured slowly into A, stirred for another 30 min, and the resulting suspension transferred into a 25 mL Teflon-lined stainless steel autoclave, which was then heated at 160°C for 12 h. After cooling to room temperature, the solid precipitate was filtered, washed with ethyl alcohol and distilled water 3–5 times, and dried at 60°C for 6 h.

2.2.3. Synthesis of Q-Bi_2WO_6

The Q-Bi_2WO_6 catalyst was obtained by a reported method [22]. Here, 0.5 mmol (0.2425 g) of $Bi(NO_3)_3 \cdot 5H_2O$ and 0.25 mmol (0.0824 g) of $Na_2WO_4 \cdot 2H_2O$ was dissolved in 40 mL of deionized water for 30 min. The mixed solution was then stirred with the addition of 3 g of Na_2SO_4 to complete dissolution and, then, 5 M H_2SO_4 used to adjust the pH to 1. The resulting mixture was transferred to a 100 mL high-pressure reaction kettle, heated at 180°C for 24 h, and naturally cooled to room temperature. Finally, the solid precipitate was filtered, washed with ethyl alcohol and distilled water 3–5 times, and dried at 60°C for 6 h.

2.2.4. Synthesis of W-Bi_2WO_6

The W-Bi_2WO_6 catalyst was obtained by a reported method [23]. Here, 0.002 mol of $Bi(NO_3)_3 \cdot 5H_2O$ and 0.001 mol of $Na_2WO_4 \cdot 2H_2O$ was dissolved in 20 mL of acetic acid and 20 mL of distilled water, respectively. Then, the mixed solution was adjusted to pH 7 by adding 1 M NaOH solution

and adding distilled water to 70 mL. The solution was transferred after mixing range to a 100 mL high-pressure reaction kettle, reacted at 200°C for 24 h, and naturally cooled to room temperature. The resulting precipitate was collected, washed several times with distilled water and ethanol, and dried in a drying oven at 60°C for 8 h to obtain the final Bi_2WO_6 products.

2.3. Characterization

Crystal structures of photocatalysts were characterized on a Rigaku D/max 2500 X-ray diffractometer (XRD; Rigaku, Corp., Tokyo, Japan) with Cu-K$_\alpha$ (λ = 0.15418 nm) radiation. Morphologies and microstructures of the samples were investigated first by a field emission-scanning electron microscopy (FE-SEM; NOVA Nano SEM 230, FEI Co., Hillsboro, OR, USA) and a high-resolution transmission electron microscope (Tecnai G$_2$ F$_{20}$, FEI Co., USA). UV-Vis diffuse reflectance spectra were recorded on a JASCO V-550/V-570 UV-vis spectrophotometer (DRS; JASCO, Corp., Tokyo, Japan) fitted with an integrating sphere accessory. The chemical states and surface chemical composition were verified by an ESCALAB 250 XI XPS spectroscope using an Al-K$_\alpha$ X-ray source (Thermo Fisher Scientific Inc., Pittsburgh, PA, USA). Photoluminescence (PL) spectra were measured on a Hitachi F-4600 fluorescence spectrophotometer (Hitachi Instruments, Inc., Tokyo, Japan; λ_{ex}, 280 nm) at room temperature. Prepared photocatalysts were dried and degassed at 90°C and 200°C, respectively, before Brunauer–Emmett–Teller (BET) measurements. The BET specific surface area was calculated from adsorption data in the P/P_0 range of 0.05–1, and P/P_0 = 0.99 was selected as a reference for obtaining the pore volume.

2.4. Photo-degradation experiments

Catalyst photocatalytic activity was evaluated by stimulating RhB degradation in a sealed photochemical reactor with a light source (450 W Xe lamp and 420 nm cut-off filter). A mass of 0.1 g of the photocatalyst was added to 100 mL of RhB solution (20 mg/L). The mixed solution was put into the reaction device and stirred magnetically in darkness for 30 min. A 2 mL aliquot of the reaction solution was taken every 15 min to assess the equilibrium state in terms of photocatalyst adsorption and desorption. After 30 min, the Xe light source was turned on to allow photocatalytic reactions and samples were taken 33every 15 min until the reaction reached equilibrium. Solid photocatalytic powder was removed by centrifugation and its absorbance detected at 357 nm, the maximum absorption peak. The measured values were converted into the concentration of target pollutants and the degradation rate of target pollutants at different times was calculated.

3. Results and discussion

3.1. Structure and morphology of synthesized Bi_2WO_6 catalysts

The diffraction peaks of the photocatalysts corresponded well with pristine orthorhombic Bi_2WO_6 (*a* = 5.457 *a*, *b* = 5.457 *a*, *c* = 5.438 *a*; JCPDS No. 39-0256; Fig. 1). The distinct
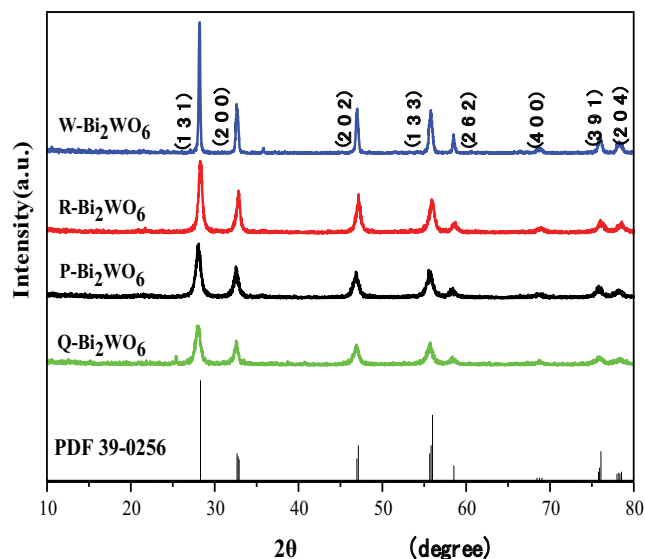
Fig. 1. XRD patterns of the four Bi_2WO_6 catalysts.

diffraction peaks at 2θ = 28.30°, 32.79°, 47.14°, 55.99°, 75.92°, 78.53°, and 87.50° were attributed to the lattice planes (131), (200), (202), (133), (391), (204), and (462), respectively.

From the bottom up along the *y*-axis, it was found that the characteristic peak strength of Bi_2WO_6 gradually increased and crystallinity also increased (Fig. 1). Also, there were no other peaks and the peak intensity high, indicating that the prepared photocatalyst had good crystallinity and was high-purity orthorhombic Bi_2WO_6.

The W-Bi_2WO_6 catalyst possessed a complete and unified hexahedral nanoparticle structure with small and uniform particle size and grain sizes between 400 and 450 nm (Fig. 2a). Almost all grains in the sample were flower spherules (R-Bi_2WO_6) with diameters of 2.5–3.0 μm (Fig. 2b). Also, high magnification SEM of the sample showed that a single Bi_2WO_6 particle was assembled in interspersed lamellar structures. The synthesis of the bird's nest catalyst (Q-Bi_2WO_6) grains was observed to be ~1–2 μm in diameter (Fig. 2c) and showed dispersed massive structures of different sizes with particle size ranging from 100–50 μm (Fig. 2d). From SEM, the massive particle (P-Bi_2WO_6) size had a wide range and the small particle size of 100 nm had a wide distribution, with increased specific surface area, which would make pollutant transfer speeds faster, provide more active sites, improve the photon capture rate, hinder the recombination of photogenerated electrons and holes, and thus enhance catalytic activity. Therefore, it was speculated that the block catalyst had better catalytic activity.

N$_2$ adsorption experiments provided information on the materials' textural properties (Fig. 3). The photocatalytic degradation of organic dyes was related to the active sites for photocatalytic reactions. The more photocatalytic active sites there were, the larger the contact area between the photocatalyst and organic dye or pollutant was, which made the photocatalytic activity of the material higher. Active sites of photocatalysis reaction were directly related to the specific surface area of the material itself. These samples
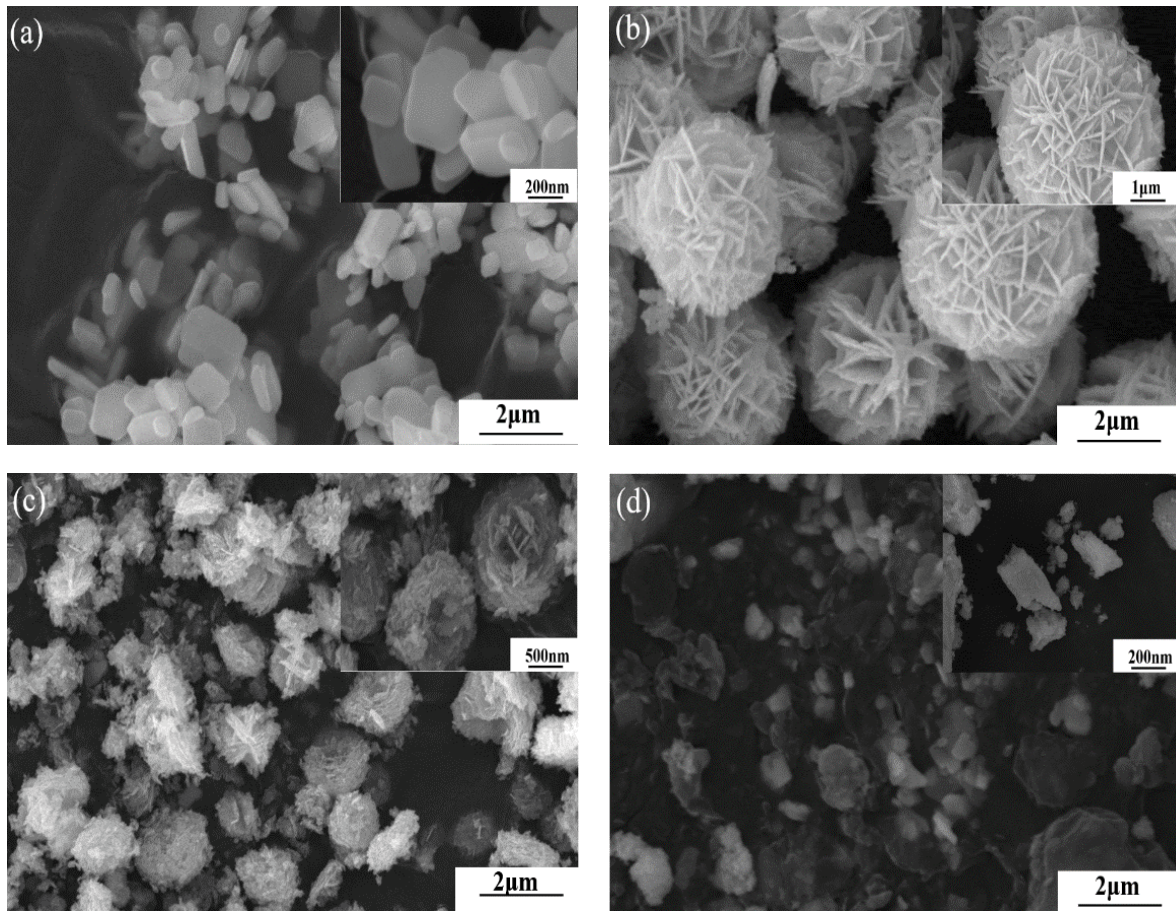
Fig. 2. SEM images of prepared (a) W-Bi$_2$WO$_6$, (b) R-Bi$_2$WO$_6$, (c) Q-Bi$_2$WO$_6$, and (d) P-Bi$_2$WO$_6$.

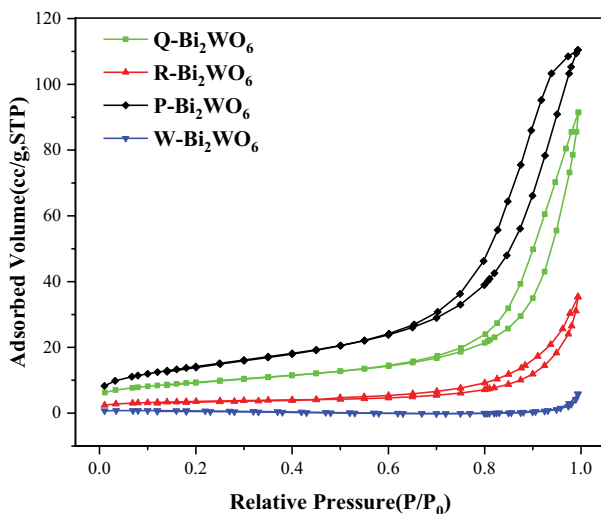Fig. 3. N$_2$ adsorption–desorption isotherm curve of Bi$_2$WO$_6$ structures.

showed type IV isotherms, reflecting the existence of mesopores between the nanosheets (Fig. 3). There were differences observed in the size of the hysteresis rings by carefully examining the adsorption and desorption imbalance of the four groups of isotherms, which reflected differences in the distribution of specific surface area and pore diameters among the four catalysts. The BET surface areas of P-Bi$_2$WO$_6$, Q-Bi$_2$WO$_6$, R-Bi$_2$WO$_6$, and W-Bi$_2$WO$_6$ were 50.5889, 32.3735, 11.7351, and 1.5490 m^2/g, respectively. P-Bi$_2$WO$_6$ had the largest specific surface area of these photocatalysts, which could supply more surface active sites and make charge carrier transport more available, leading to an enhancement of photocatalytic performance [24].

The chemical state and surface chemical composition of Bi$_2$WO$_6$ were verified by XPS (Fig. 4). In the overall spectral scan, Bi$_2$WO$_6$ displayed peaks of four primary elements, including Bi, W, O, and C (C derived from adventitious carbon on material surfaces, Fig. 4a).

XPS signals at 37.30 and 35.20 eV corresponded to W-4$f^{5/2}$ and W-4$f^{7/2}$ respectively, suggesting that Bi element could be ascribed to W^{+6}, which was consistent with the literature (Fig. 4b) [25]. The combined energy of W-Bi$_2$WO$_6$ and Q-Bi$_2$WO$_6$ as Bi-4$f^{5/2}$ and Bi-4$f^{7/2}$ were 164.00 and 158.70 eV, respectively. Furthermore, P-Bi$_2$WO$_6$ and R-Bi$_2$WO$_6$'s Bi-4$f^{5/2}$ and Bi-4$f^{7/2}$ binding energies were 164.20 and 158.90 eV, respectively, which suggested that Bi existed in the form of Bi^{+3} (Fig. 4c) [26]. The main peak at 529.6 eV corresponded with the Bi-O bond in (Bi$_2$O$_2$)$^{2+}$ slabs that have lattice oxygen and a peak at 530.8 eV due to hydroxyl groups (Fig. 4d) [25].
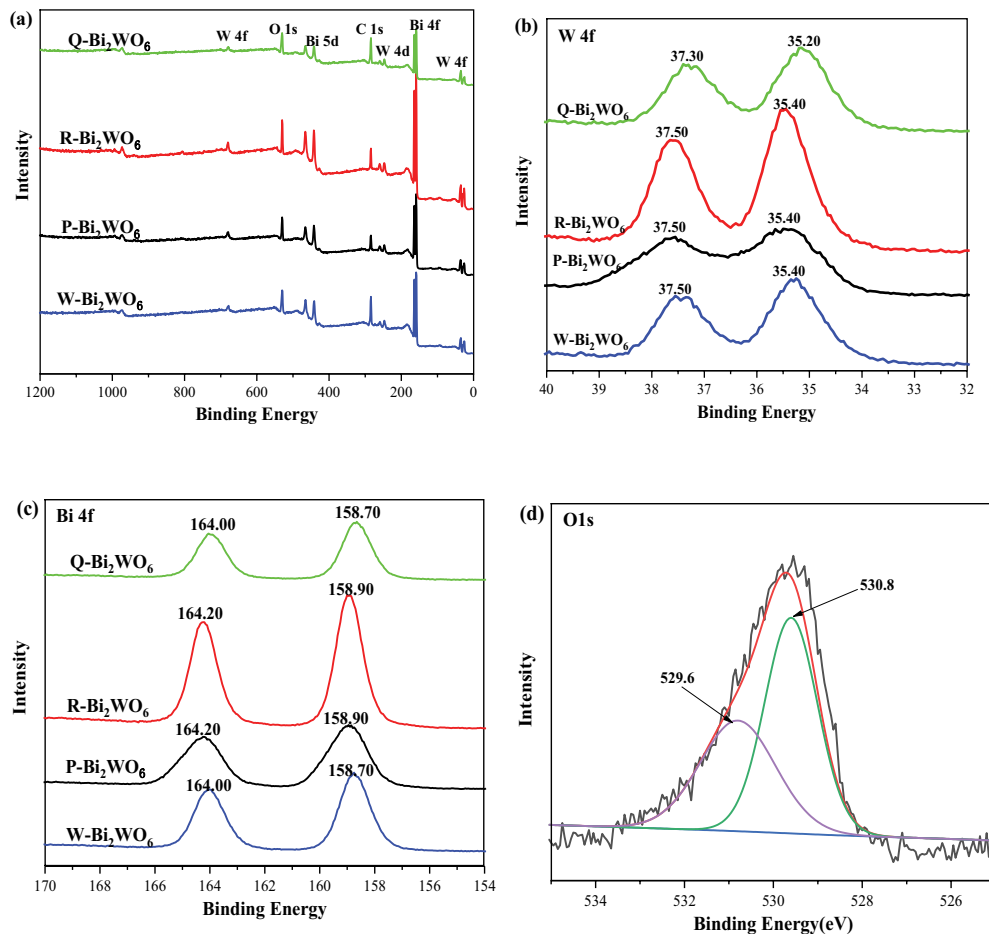
Fig. 4. XPS spectra of full spectrum (a), W-4*f* (b), Bi-4*f* (c), and O-1s (d) of prepared Bi_2WO_6 samples.

3.2. Optical properties and band structures of Bi_2WO_6 catalysts

To investigate the photoresponse range of the samples, the light absorption properties of these semiconductor photocatalysts were evaluated by UV-Vis spectrophotometry over 200–800 nm (Fig. 5). The catalyst had a certain amount of light absorption in the UV-Vis light range, which meant that the sample responded well to UV-Vis absorption [12]. $P-Bi_2WO_6$ had the best photocatalytic activity among the four samples, followed closely by $R-Bi_2WO_6$, $Q-Bi_2WO_6$, and $W-Bi_2WO_6$.

As the forbidden width of a semiconductor affected the light absorption edge of the catalyst, the Kubelka–Munk Eq. (1) was used here to estimate the band gap width of catalyst samples.

$$\alpha hv = A\left(hv - Eg\right)^{n/2} \qquad (1)$$

where α is the absorption coefficient; *h* Planck's constant; *v* the light frequency; for example, the forbidden bandwidth; a constant, usually 1; *n* determined by the type of light transition in a typical semiconductor, usually 1 [25,27]. The Kubelka–Munk equation was used to determine the intersection of the tangent line and abscissa at the inflection point, thus obtaining the forbidden band

width (Fig. 5a) [28]. The catalysts' forbidden band width was plotted and calculated from the tangent, being 2.45, 2.50, 2.59, and 2.62 for $P-Bi_2WO_6$, $R-Bi_2WO_6$, $Q-Bi_2WO_6$, and $W-Bi_2WO_6$, respectively. It was concluded from these results that, with decreased band width, the red shift of the catalyst absorption band edge increased its visible light response (Fig. 5b) [29].

To further clarify the relative positions of the VB and CB of the samples, the total densities of the VB state spectra were collected [13]. The VB tops of the four Bi_2WO_6 species were obtained by linear extrapolation, showing an order of $P-Bi_2WO_6$, $R-Bi_2WO_6$, $Q-Bi_2WO_6$, and $W-Bi_2WO_6$ (2.71, 2.59, 2.50, and 2.11 eV, respectively; Fig. 6a). According to the estimated results, the position of the blocky VB was concluded to be the highest and its oxidation performance the best, which corresponded to the UV-Vis diffuse reflection analytical results. The band gap of bulk Bi_2WO_6 hybrids was seen to decrease and the potential at the VB top shifted to a higher positive potential, which ensured that photoinduced holes had enough potential to oxidize target reactants, such as organic matter and water [30]. Finally, as the VB position increased, oxidation activity increased in turn. The apparent CB potentials of the prepared samples were calculated by the means of the corresponding VB potential and measured band gaps and the energy level distributions of CB and
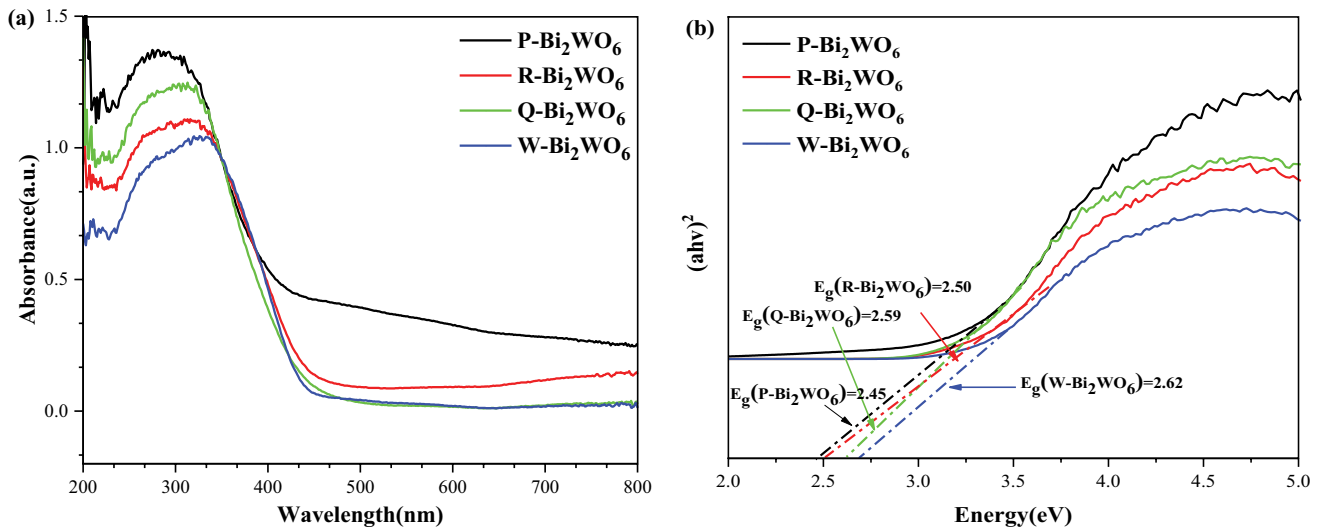
Fig. 5. (a) UV-Vis diffused reflection spectra and (b) Tauc plots of prepared samples.
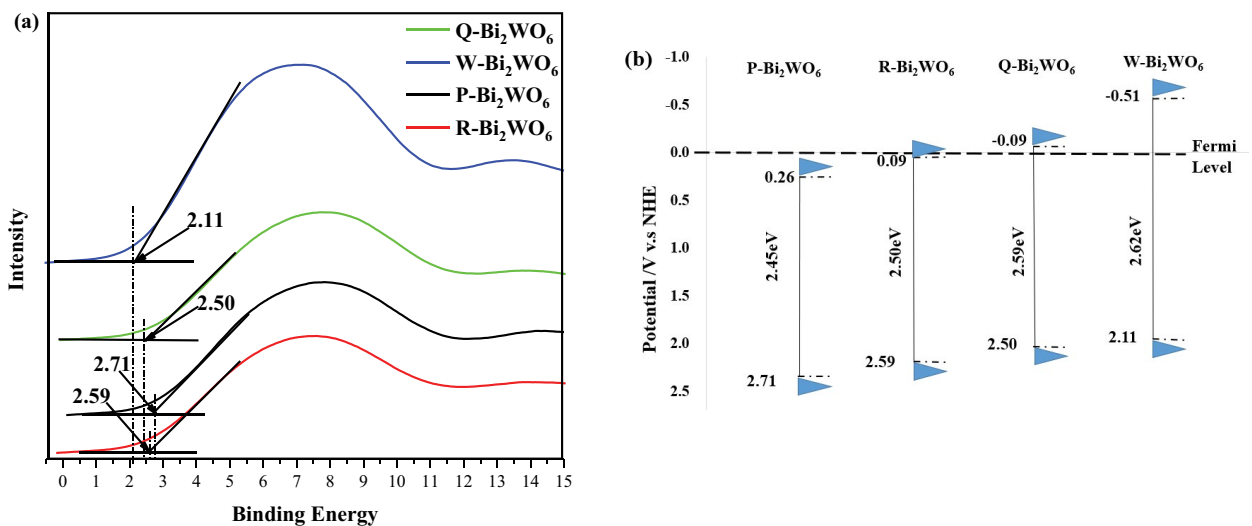

Fig. 6. VB XPS spectra (a) and energy level distributions of CB and VB (b) of the P-Bi_2WO_6, R-Bi_2WO_6, Q-Bi_2WO_6, and W-Bi_2WO_6 samples.

VB summarized and illustrated in Fig. 6b. The bandgap of the P-Bi_2WO_6 was observed to be reduced, with the potential of the VB top shifted to a more positive potential, which ensured sufficient potential for photoexcited holes to oxidize target reactants, such as organics and water.

PL spectra were used to analyze the migration, trapping, and recombination of photocarriers in bismuth tungstate photocatalysts. The emission peak in the PL spectrum was caused by the recombination of photogenerated charge carriers [31]. Therefore, the higher PL emission peaks were the easier the combination of carriers [32]. Fig. 7 shows The PL spectra of Bi_2WO_6 catalyst (λ_{ex} = 280 nm) showed that the PL radiation peak intensity was in the order of W-Bi_2WO_6 > Q-B i$_2WO_6$ > R-Bi_2WO_6 > P-Bi_2WO_6. These results were in accord with the variation trend of UV-Vis and VB results. In other

words, a larger absorption band edge and higher position of the blocky VB resulted in weaker PL peaks and stronger photocatalytic activity [33].

3.3. Visible light-driven catalytic activity of Bi_2WO_6 catalysts

Using RhB as the target pollutant, degradation experiments of the present Bi_2WO_6 series of photocatalysts with different morphologies were performed under a Xe light source and the corresponding adsorption performances also assessed.

The adsorption and saturation time of different catalysts were all 30 min and the RhB concentration remained almost unchanged during the period from 30 to 180 min (Fig. 8). The pure adsorption curve showed that the catalysts'

adsorption performance was in the order of R-Bi_2WO_6 > Q-Bi_2WO_6 > P-Bi_2WO_6 > W-Bi_2WO_6.

Photocatalytic degradation of RhB involves two main pathways: a de-ethylation mechanism and auto sensitization degradation. The first mechanism is the continuous decomposition of RhB to produce intermediates, while the second mechanism involves the absorption of UV light by RhB to reach singlet and triplet states and the release of electrons when the electrons return to a stable energy state. This electron is transferred directly to the conduction band of a semiconductor [34]. The former path gradually shifted the position to the blue region as the ethyl groups were removed one by one, but the latter path accompanied the disappearance of the visible absorption band, with the peak position unchanged [8]. The UV-Vis spectrum of photocatalytic degradation is shown in Fig. 9. RhB dye contains two N-ethyl

groups at each side of the xanthene ring, which is stable in aqueous solution under visible-light irradiation (Fig. 9a) [35]. However, it can be seen that tetramethylrhodamine has a major absorption band at 553 nm (Fig. 9b). Under the exposure of visible light at 420 nm, the absorption of RhB/Bi_2WO_6 aqueous solution was weakened, which was accompanied by a wavelength shift towards a shorter wavelength. Under visible illumination, the dye changed from its original red to light greenish-yellow. This maximum absorbance blue shift has been shown to be caused by the formation of de-ethylated intermediates during the photocatalytic degradation of RhB [36]. According to the standard spectrum, completely de-ethylated RhB molecule has a main absorption band at a maximum of 506 nm. Here, color loss of the dispersion (after 90 min exposure) indicated that at least some of the dye's color structure had been destroyed [15]. By comparing the
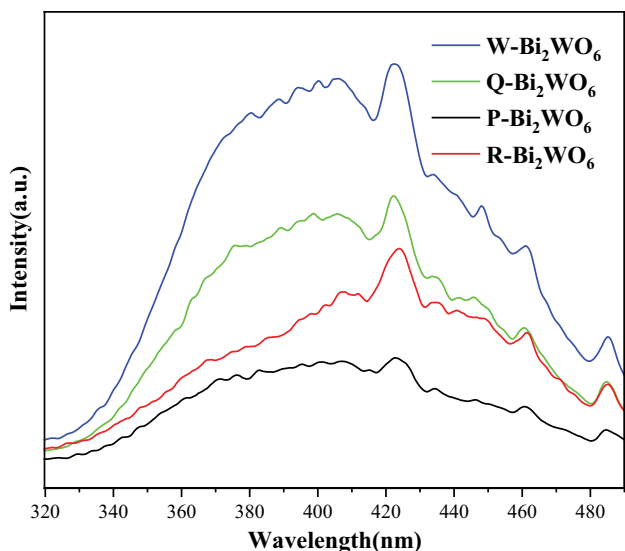

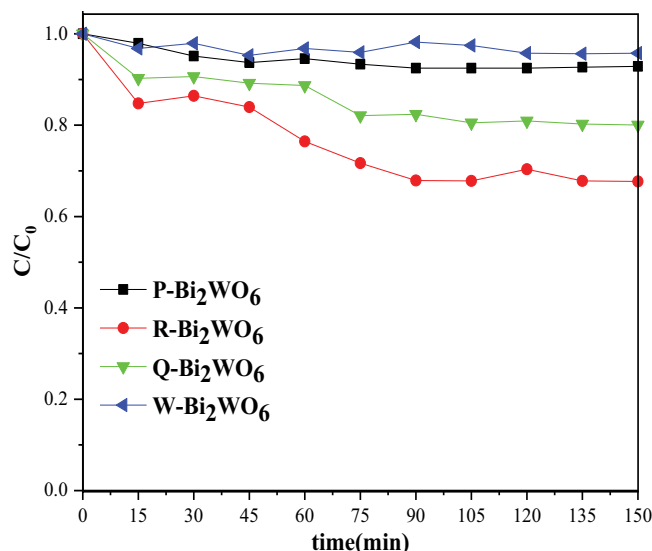Fig. 7. Room-temperature PL spectra of Bi_2WO_6 catalysts.

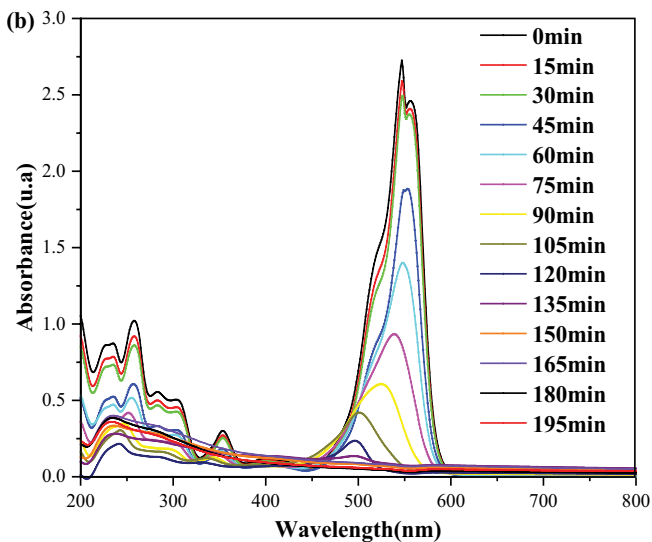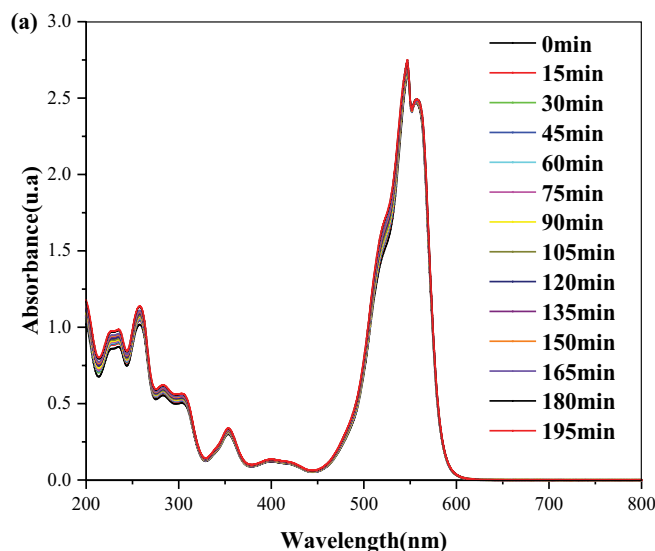Fig. 8. Adsorption performance curves of the catalysts.

Fig. 9. Stability of the RhB under UV light (a) UV-Vis spectra of the reaction solution with P-Bi_2WO_6 (b).

spectra after 60 min with the initial spectra, ~53.8% of RhB formed rhodamine after complete demethylation, while the rest degraded by destroying conjugated structures.

The results showed that the self-degradation rates of RhB in blank experimental groups were not high, at 3.0%. P-Bi$_2$WO$_6$ exhibited the best catalytic activity and degraded 20 mg/L RhB over 150 min (lighted for 120 min) at a rate of 94.40% (Fig. 10a). The change curve of the reaction rate constant *k* of the catalyst in RhB degradation by visible light is shown in Fig. 10b. The degradation rate is another method for evaluating photocatalytic activity. The higher *k* value, the better the photocatalytic performance of the catalyst. According to the modified Langmuir–Hinshelwood kinetic model, the photocatalytic degradation reaction was described by first-order kinetic, Eqs. (2) and (3)

$$\frac{dc}{dt} = K_c C \tag{2}$$

$$\ln\left(\frac{C_0}{C_t}\right) = K_c t \tag{3}$$

where K_c is the first-order reaction kinetic rate constant. Curve fitting showed that RhB photocatalytic degradation by the four catalysts confirmed to first-order reaction kinetics (Fig. 10b). The results were consistent with those shown in Fig. 10a.

It was confirmed again that the higher the valence band position and the narrower the band gap were, the faster the migration of photogenic holes in the VB, which increased photocatalytic activity. Also, specific surface area, grain size, and structural morphology can affect the photocatalytic performance of materials [37]. P-Bi$_2$WO$_6$ catalyst had the smallest size and largest specific surface area, which provided more unsaturated active sites and adsorbed more dye, which enhanced its photocatalytic activity. Although the hierarchical structures of R-Bi$_2$WO$_6$ and Q-Bi$_2$WO$_6$ both

consisted of numerous Bi$_2$WO$_6$ nanosheets, the VB position of R-Bi$_2$WO$_6$ was higher and the forbidden bandwidth narrower, which made photogenic hole migration in the VB faster. This series of effects yielded the photocatalytic activity of R-Bi$_2$WO$_6$ stronger than that of Q-Bi$_2$WO$_6$ catalyst. The W-Bi$_2$WO$_6$ catalyst had the lowest VB and the highest forbidden bandwidth (Fig. 6b). In this catalyst, due to the interaction of the Coulomb force, the electron-hole recombination rate was high, such that the photocatalytic and oxidation activities were the worst.

The stability of the P-Bi$_2$WO$_6$ was also investigated by recycling the photocatalyst for RhB degradation (20 mg/L) under visible-light irradiation (Fig. 11). When the catalyst was reused four times, the removal rate of RhB (92.48%) decreased compared with the first result (94.72%), which was related to the shedding of a small amount of powder
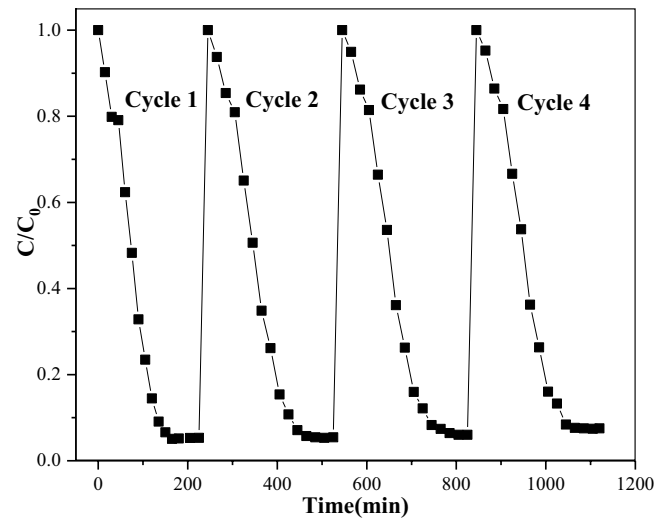

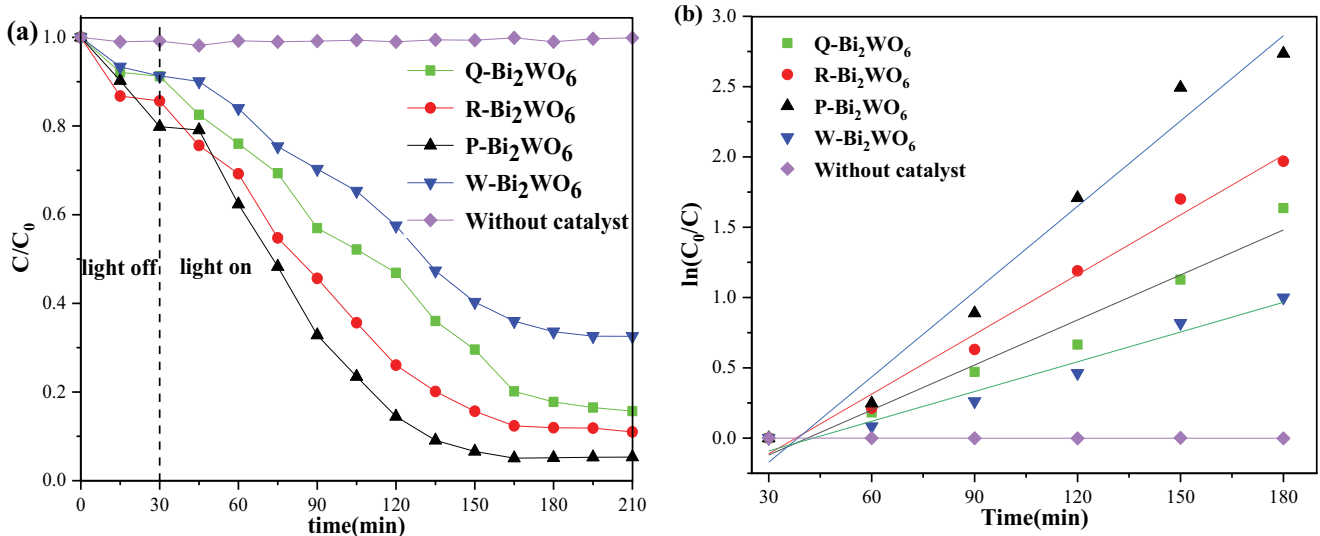Fig. 11. Cycling runs of the photo-degradation for RhB with P-Bi$_2$WO$_6$.

Fig. 10. Photodegradation for RhB with Bi$_2$WO$_6$ catalysts under visible-light irradiation (a) and pseudo-first-order kinetics of the photocatalysts (b).

catalyst in each experiment. Also, the RhB degradation rate was gradually decreased in each repeated cycle, which was speculated to be related to RhB adsorption on the catalyst. As the compound catalyst was simply stirred and cleaned with distilled water several times after each experiment and the photocatalytic experiment was conducted again after drying of the catalyst, there might have been incomplete cleaning of the catalyst, which led to the degradation rate of RhB being decreased in subsequent cycles. In conclusion, the P-Bi$_2$WO$_6$ has relatively stable photocatalytic activity under visible light conditions.

4. Conclusions

In summary, P-Bi$_2$WO$_6$, R-Bi$_2$WO$_6$, Q-Bi$_2$WO$_6$, and W-Bi$_2$WO$_6$ photocatalysts were successfully synthesized using hydrothermal methods. The VB height played an important role in the formation of Bi$_2$WO$_6$ microstructures. Under visible-light irradiation, P-Bi$_2$WO$_6$ photocatalyst effectively degraded RhB, which was ascribed to its special microstructure, relatively large surface area, and especially its higher VB. At the same time, this theory and study provided a supported theoretical basis for future research on the relationship between VB position and catalytic performance.

Acknowledgement

References

[1] M. Punzi, A. Anbalagan, R.A. Borner, B.-M. Svensson, M. Jonstrup, B. Mattiasson, Degradation of a textile azo dye using biological treatment followed by photo-Fenton oxidation: evaluation of toxicity and microbial community structure, Chem. Eng. J., 270 (2015) 290–299.

[2] H. Xu, B. Yang, Y.B. Liu, F. Li, C.S. Shen, C.Y. Ma, Q. Tian, X.S. Song, W. Sand, Recent advances in anaerobic biological processes for textile printing and dyeing wastewater treatment: a mini-review, World J. Microbiol. Biotechnol., 34 (2018) 9.

[3] M. Hojamberdiev, Z.C. Kadirova, E. Zahedi, D. Onna, M.C. Marchi, G. Zhu, N. Matsushita, M. Hasegawa, S.A. Bilmes, K. Okada, Tuning the morphological structure, light absorption, and photocatalytic activity of Bi$_2$WO$_6$ and Bi$_2$WO$_6$-BiOCl through cerium doping, Arabian J. Chem., 13 (2020) 2844–2857.

[4] M. Zargazi, M.H. Entezari, Sonochemical vs. hydrothermal synthesis of bismuth tungstate nanostructures: photocatalytic, sonocatalytic, and sonophotocatalytic activities, Ultrason. Sonochem., 51 (2019) 1–11.

[5] W. Wang, P. Serp, P. Kalck, C.G. Silva, J.L. Faria, Preparation and characterization of nanostructured MWCNT-TiO$_2$ composite materials for photocatalytic water treatment applications, Mater. Res. Bull., 43 (2008) 958–967.

[6] Y. Li, H. Zhang, P. Liu, D. Wang, Y. Li, H. Zhao, Cross-linked g-C$_3$N$_4$/rGO nanocomposites with tunable band structure and enhanced visible-light photocatalytic activity, Small, 9 (2013) 3336–3344.

[7] K. Zhang, J. Wang, W. Jiang, W. Yao, H. Yang, Y. Zhu, Self-assembled perylene diimide based supramolecular heterojunction with Bi$_2$WO$_6$ for efficient visible-light-driven photocatalysis, Appl. Catal., B, 232 (2018) 175–181.

[8] D. Liu, J. Zhang, C. Li, X. Zhang, X. Chen, F. Wang, M. Shi, R. Li, C. Li, In-situ fabrication of atomic charge transferring path for constructing heterojunction photocatalysts with hierarchical structure, Appl. Catal., B, 248 (2019) 459–465.

[9] L. Liu, Y. Qi, J. Lu, S. Lin, W. An, J. Hu, Y. Liang, W. Cui, Dramatic activity of a Bi$_2$WO$_6$@g-C$_3$N$_4$ photocatalyst with a core@shell structure, RSC Adv., 5 (2015) 99339–99346.

[10] J. He, W. Wang, F. Long, Z. Zou, Z. Fu, Z. Xu, Hydrothermal synthesis of hierarchical rose-like Bi$_2$WO$_6$ microspheres with high photocatalytic activities under visible-light irradiation, Mater. Sci. Eng., B, 177 (2012) 967–974.

[11] M. Tachibana, Thermal conductivity of Aurivillius compounds Bi$_2$WO$_6$, SrBi$_2$Ta$_2$O$_9$, and Bi$_4$Ti$_3$O$_{12}$, Solid State Commun., 211 (2015) 1–3.

[12] B.Y. Alfaifi, A.A. Tahir, K.G.U. Wijayantha, Fabrication of Bi$_2$WO$_6$ photoelectrodes with enhanced photoelectrochemical and photocatalytic performance, Sol. Energy Mater. Sol. Cells, 195 (2019) 134–141.

[13] H. Zhou, Z. Wen, J. Liu, J. Ke, X. Duan, S. Wang, Z-scheme plasmonic Ag decorated WO$_3$/Bi$_2$WO$_6$ hybrids for enhanced photocatalytic abatement of chlorinated-VOCs under solar light irradiation, Appl. Catal., B, 242 (2019) 76–84.

[14] T. Saison, P. Gras, N. Chemin, C. Chanéac, O. Durupthy, V. Brezová, C. Colbeau-Justin, J.-P. Jolivet, New insights into Bi$_2$WO$_6$ properties as a visible-light photocatalyst, J. Phys. Chem. C, 117 (2013) 22656–22666.

[15] H. Fu, C. Pan, W. Yao, Y. Zhu, Visible-light-induced degradation of rhodamine B by nanosized Bi$_2$WO$_6$, J. Phys. Chem. B, 109 (2005) 22432–22439.

[16] A. Zhu, Q. Zhao, X. Li, Y. Shi, BiFeO$_3$/TiO$_2$ nanotube arrays composite electrode: construction, characterization, and enhanced photoelectrochemical properties, ACS Appl. Mater. Interfaces, 6 (2014) 671–679.

[17] H. Sun, Z. Tian, G. Zhou, J. Zhang, P. Li, Exploring the effects of crystal facet in Bi$_2$WO$_6$/BiOCl heterostructures on photocatalytic properties: a first-principles theoretical study, Appl. Surf. Sci., 469 (2019) 125–134.

[18] M. Ren, F. Teng, Y. Yang, Y. Zhai, W. Gu, Z. Liu, Z. Liu, Y. Teng, Influence of O/F ratio on oxygen defect and photochemical properties of BixOyFz, Mater. Des., 131 (2017) 402–409.

[19] Y. Yang, F. Teng, Y. Kan, L. Yang, Z. Liu, W. Gu, A. Zhang, W. Hao, Y. Teng, Investigation of the charges separation and transfer behavior of BiOCl/BiF$_3$ heterojunction, Appl. Catal., B, 205 (2017) 412–420.

[20] S. Zhong, F. Zhang, B. Yu, P. Zhao, L. Jia, S. Zhang, Synthesis of PVP-Bi$_2$WO$_6$ photocatalyst and degradation of tetracycline hydrochloride under visible light, J. Mater. Sci. - Mater. Electron., 27 (2015) 3011–3020.

[21] G.-Y. Zhang, Y. Feng, Q.-S. Wu, Y.-Y. Xu, D.-Z. Gao, Facile fabrication of flower-shaped Bi$_2$WO$_6$ superstructures and visible-light-driven photocatalytic performance, Mater. Res. Bull., 47 (2012) 1919–1924.

[22] H. Jinyun, W. Weimin, Z. Linlang, Z. Zhengguang, F. Zhengyi, X. Zhe, Morphology controlled synthesis and characterization of Bi$_2$WO$_6$ photocatalysts, J. Wuhan Univ. Technol. (Mater. Sci. Ed.)., 28 (2013) 231–234.

[23] F. Wang, H. Yang, H. Zhang, J. Su, X. Wang, Electrochemical performance of morphologically different Bi$_2$WO$_6$ nanostructures synthesized via a hydrothermal route, J. Electron. Mater., 46 (2016) 182–187.

[24] Z. Sun, J. Guo, S. Zhu, J. Ma, Y. Liao, D. Zhang, High photocatalytic performance by engineering Bi$_2$WO$_6$ nanoneedles onto graphene sheets, RSC Adv., 4 (2014) 27963–27970.

[25] D. Jiang, T. Wang, Q. Xu, D. Li, S. Meng, M. Chen, Perovskite oxide ultrathin nanosheets/g-C$_3$N$_4$ 2D-2D heterojunction photocatalysts with significantly enhanced photocatalytic activity towards the photodegradation of tetracycline, Appl. Catal., B, 201 (2017) 617–628.

[26] D. Jiang, W. Ma, P. Xiao, L. Shao, D. Li, M. Chen, Enhanced photocatalytic activity of graphitic carbon nitride/carbon nanotube/Bi$_2$WO$_6$ ternary Z-scheme heterojunction with carbon nanotube as efficient electron mediator, J. Colloid Interface Sci., 512 (2018) 693–700.

[27] J. Ke, J. Liu, H. Sun, H. Zhang, X. Duan, P. Liang, X. Li, M.O. Tade, S. Liu, S. Wang, Facile assembly of Bi$_2$O$_3$/Bi$_2$S$_3$/MoS$_2$ n-p

heterojunction with layered n-Bi$_2$O$_3$ and p-MoS$_2$ for enhanced photocatalytic water oxidation and pollutant degradation, Appl. Catal., B, 200 (2017) 47–55.

[28] I. Zumeta-Dubé, J.-L. Ortiz-Quiñonez, D. Díaz, C. Trallero-Giner, V.-F. Ruiz-Ruiz, First order raman scattering in bulk Bi2S3 and quantum dots: reconsidering controversial interpretations, J. Phys. Chem. C, 118 (2014) 30244–30252.

[29] N. Lv, Y. Li, Z. Huang, T. Li, S. Ye, D.D. Dionysiou, X. Song, Synthesis of GO/TiO$_2$/Bi$_2$WO$_6$ nanocomposites with enhanced visible-light photocatalytic degradation of ethylene, Appl. Catal., B, 246 (2019) 303–311.

[30] J. Xia, S. Yin, H. Li, H. Xu, Y. Yan, Q. Zhang, Self-assembly and enhanced photocatalytic properties of BiOI hollow microspheres via a reactable ionic liquid, Langmuir, 27 (2011) 1200–1206.

[31] J. Wang, L. Tang, G. Zeng, Y. Deng, H. Dong, Y. Liu, L. Wang, B. Peng, C. Zhang, F. Chen, OD/2D interface engineering of carbon quantum dots modified Bi$_2$WO$_6$ ultrathin nanosheets with enhanced photoactivity for full-spectrum light utilization and mechanism insight, Appl. Catal., B, 222 (2018) 115–123.

[32] C. Yu, Z. Wu, R. Liu, D.D. Dionysiou, K. Yang, C. Wang, H. Liu, Novel fluorinated Bi$_2$MoO$_6$ nanocrystals for efficient photocatalytic removal of water organic pollutants under different light source illumination, Appl. Catal., B, 209 (2017) 1–11.

[33] H. Huang, X. Han, X. Li, S. Wang, P.K. Chu, Y. Zhang, Fabrication of multiple heterojunctions with tunable visible-light-active photocatalytic reactivity in BiOBr-BiOI full-range composites based on microstructure modulation and band structures, ACS Appl. Mater. Interfaces, 7 (2015) 482–492.

[34] H.A. Ahsaine, M. Ezahri, A. Benlhachemi, B. Bakiz, S. Villain, F. Guinneton, J.R. Gavarri, Novel Lu-doped Bi$_2$WO$_6$ nanosheets: synthesis, growth mechanisms and enhanced photocatalytic activity under UV-light irradiation, Ceram. Int., 42 (2016) 8552–8558.

[35] Q. Wang, C. Chen, D. Zhao, W. Ma, J. Zhao, Change of adsorption modes of dyes on fluorinated TiO$_2$ and its effect on photocatalytic degradation of dyes under visible irradiation, Langmuir, 24 (2008) 7338–7345.

[36] H. Park, W. Choi, Photocatalytic reactivities of Nafion-coated TiO$_2$ for the degradation of charged organic compounds under UV or visible light, J. Phys. Chem. B, 109 (2005) 11667–11674.

[37] S. Adhikari, S. Selvaraj, D.-H. Kim, Construction of hetero-junction photoelectrode via atomic layer deposition of Fe$_2$O$_3$ on Bi$_2$WO$_6$ for highly efficient photoelectrochemical sensing and degradation of tetracycline, Appl. Catal., B, 244 (2019) 11–24.